Mass log-stable distribution of fragments in liquid–liquid jet fragmentation based on a two-step cascade between viscous shear instability and Rayleigh–Taylor instability

Nicolas Rimbert [a,*], Miloud Hadj-Achour [a], Bowen Ji [a], Gagan Kewalramani [a], Alexandre Labergue [a], Yvan Dossmann [a], Michel Gradeck [a], Pascal Piluso [b], Renaud Meignen [c]

[a] LEMTA, CNRS Universite de Lorraine, Vandoeuvre-les-Nancy, 54518, France
[b] CEA DES\IRESNE\DTN\SMTA\LEAG, Cadarache, France
[c] Institut de Radioprotection et de Surete Nucleaire (IRSN), Saint Paul Lez Durance, France

ARTICLE INFO

MSC:
00-01
99-00

Keywords:
Liquid/Liquid fragmentation
Instability
Cascade mechanism
Log-stable laws

ABSTRACT

This work is devoted to the study of liquid–liquid fragmentation. It contains both an experimental part and a theoretical part. In the experimental part, a low-melting point liquid metal jet is injected into a water pool. High-speed shadowgraph method is used to measure the jet velocity and to observe the dynamics of the fragmentation. Thereafter, the solidified fragments are sieved and weighted allowing to measure their mass distribution according to their size. The mass Probability Density Function (PDF) is then fitted using log-stable laws, generalization of log-normal laws. In the theoretical part, it is shown how it is possible to compute the shift parameter of the stable law considering that the droplets are mainly generated by a boundary layer stripping mechanism. Actually the computation relies on a viscous shear instability mechanism (different from classical Kelvin–Helmholtz instability) sometime called "gradient instability". The width of the distribution (or more precisely its scale parameter) is computed assuming a cascade mechanism between this first wave instability and a secondary Rayleigh–Taylor mechanism applied on the generated wave. The model is then compared to present experimental results and previously published results obtained in the field of nuclear safety studies (Fuel-Coolant Interaction or FCI). Two fitting parameters are then identified. The agreement is good when phase change and solidification effects can be neglected and qualitatively good (*i.e.* fitting parameters need to be modified) when these effects cannot be neglected.

1. Introduction

Atomization and Sprays have a wide range of applications and are now a common field of study in multiphase flow. The present paper is dedicated to the study of liquid–liquid jet fragmentation with high density ratio. The main motivation of this work is related to the understanding and modeling of the premixing stage of "Fuel-Coolant Interaction" (FCI) in the frame of severe accident in Nuclear Power Plants. This situation involves the mixing of the hot molten core (corium) interacting with surrounding cooling water. The "cold" configuration, that is presented here, cannot really be representative of the real situation where the melt reaches temperatures between 2000 and 3000 K (depending on its composition: U-Zr-Fe-O and various fission products), and thus yields an important vapor production (as well as H_2 production due to oxidation). Nevertheless, in order to be able to produce adequate modeling in the 3-phase situation, it is necessary to better understand and model the simpler situations of liquid/liquid and liquid/gas configuration. The present study is therefore devoted to the liquid/liquid case, which has been much less studied than the liquid/gas one but may bear similar mechanisms.

In the present work, overheating of the molten metal is low enough so that no vapor is ever produced. This allows using non-intrusive optical diagnostics like high-speed shadowgraphy in order to build models that could eventually be used on more realistic case (comparison will be made with previously published results). A traditional sieving methods is also employed to analyze the debris. To do so, the water temperature has been chosen so that the melt could solidify only once the fragmentation process is complete.

As liquid/liquid is expected to bear similarity with liquid/gas case, let us recall that recent advances concerns firstly the influence of intermediate ligament in the fragmentation process (Villermaux et al.,

2004), (though not really new, see Dombrowski and Johns (1963) for instance). The main result of the authors, here, is that ligament breakup dynamics lead to a Gamma distribution of the daughter droplets. However, no leads to how-to compute parameters of the Gamma distribution has been found in the general case up to now. Furthermore, this result seems to contradict Kolmogorov analysis (Kolmogorov, 1941), leading to log-normal distribution, recently modernized (Novikov and Dommermuth, 1997; Gorokhovski and Saveliev, 2003; Rimbert and Séro-Guillaume, 2004; Vallon et al., 2021). Even in the Kolmogorov frame of analysis, the computation of the parameters in the general case is still difficult though some few models do exist (Gorokhovski et al., 2009). Last, competition between classical instabilities such as Rayleigh–Taylor instability (often associated to bag-breakup) or Kelvin–Helmholtz instabilities (often associated to boundary layer stripping) is known to be fundamental in the modeling. This leads to semi-empirical models such as the so-called WAVE model (Reitz, 1987; Beale and Reitz, 1999) which are still used nowadays in commercial Computer Fluid Dynamics codes. Experimental results have also shown the importance of using a cascade of instability (Rayleigh–Taylor building up on a wave generated by viscous shear instability) in the case of an air-blast atomizer (Varga et al., 2003).

In the wake of these works, Rimbert & Séro-Guillaume (Rimbert and Séro-Guillaume, 2004) developed an extension of Kolmogorov's work to log-stable law and applied it successfully to high-Weber number (third party) spray Mass Probability Distribution Function (PDF). These laws are generalizations of log-normal laws and are sometimes known as universal multifractals (Mandelbrot, 1982; Schertzer and Lovejoy, 1987). However, in this first work, the parameters were fitted and no phenomenological explanation about their value was given. Building on Kida's work (Kida, 1991; Rimbert and Séro-Guillaume, 2003), Rimbert (2010) gave a possible explanation (self-avoiding vortex tangles related to angular momentum conservation) of the importance of log-stable law in the modeling of fine-scale structure of turbulence, but most importantly, also gave a way to compute the stability index α of the distribution ($\alpha \approx 1.7$).

Liquid–liquid studies are comparatively scarcer (*cf.* (Pilch and Erdman, 1987; Gelfand, 1996; Abe et al., 2004, 2006; Kudinov et al., 2013; Manickam et al., 2017; Li et al., 2017; Saito et al., 2017; Iwasawa and Abe, 2018) for instance) and mainly focus on severe nuclear accidents (with vapor production) and granulometry of the fragments (using mainly the Mass Median Diameter or MMD). The modeling is focused on comparing these MMD to either classical Kelvin–Helmholtz or Rayleigh–Taylor wavelengths. Moreover, the mass PDF is seldom reported precisely (*i.e.* in a table). The purpose of present work is to show how mass log-stable distribution (Rimbert and Séro-Guillaume, 2004) allows for the computation of the droplet PDF in present liquid–liquid case. The Mass PDF is found to be mainly driven by large scale instabilities in a successive manner, hereafter named "two-step cascade" : first a viscous boundary layer wave instability (Rayleigh, 1880) then more classically a Rayleigh–Taylor instability; however appearing in a subsequent cascading step (*i.e.* the corresponding new length scales are computed using the length scale generated by the first instability). It will also be shown how to compute all the relevant parameters of the distributions using the proposed phenomenology. Lastly, comparison with previously cited liquid/liquid experiments will be made whenever possible.

2. Experimental set-up

2.1. Non dimensional numbers

The four non dimensional parameters governing the hydrodynamics of the fragmentation of a liquid jet of diameter D_0 and velocity U_0 are: the (carrier) Weber number We, the Ohnesorge number Oh,

$$We = We_C = \frac{\rho_C U_0^2 D_0}{\gamma}, \qquad Oh = \frac{\mu_L}{\sqrt{D_0 \rho_L \gamma}}, \tag{1}$$

Table 1
Physical Properties of Field's metal. ρ is the density, σ is the water/liquid metal interfacial tension, k is the thermal conductivity, μ is the dynamic viscosity, L_f the fusion latent heat and C_p the heat capacity.

ρ	γ	k	μ	L_f	C_p
kg/m^3	N/m	$\frac{W}{m.K}$	Pa s	$\frac{J}{kg}$	$\frac{J}{kg\ K}$
7994	0.41	5.44	0.01	26415	300

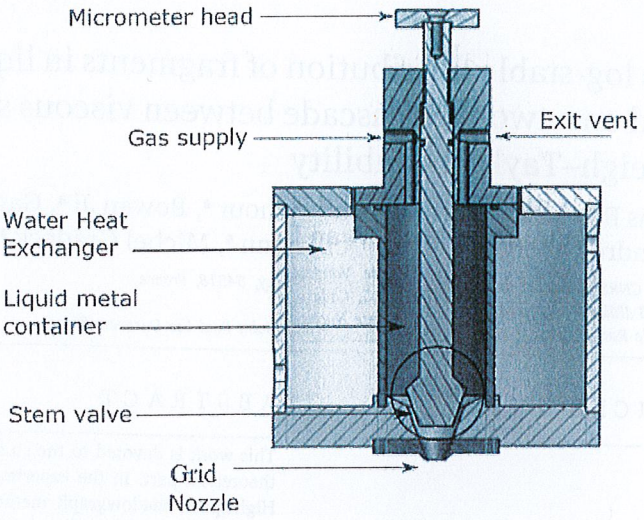

Fig. 1. GaLaD experimental Set-up.

the density ratio ρ_R and the viscosity ratio μ_R, where subscript L refers to the properties of the Liquid jet and subscript C refers to the properties of the Carrier phase.

$$\rho_R = \frac{\rho_L}{\rho_C}, \qquad \mu_R = \frac{\mu_L}{\mu_C} \tag{2}$$

In the present case, the Weber number is the main hydrodynamic parameter. Other important non dimensional parameters will be used, they are: the Reynolds numbers (for the carrier and the liquid)

$$Re_C = \frac{\rho_C U_0 D_0}{\mu_C}, \qquad Re_L = \frac{\rho_L U_0 D_0}{\mu_L} \tag{3}$$

and the liquid Weber number

$$We_L = \frac{\rho_L U_0^2 D_0}{\gamma}. \tag{4}$$

Note that $Oh = \sqrt{We_L}/Re_L$.

2.2. Set-up description

The experimental set-up is a modification of the drop-on-demand set-up used in Hadj-Achour et al. (2021), itself derived from Amirzadeh et al. (2013). The liquid metal injector is represented on Figs. 1 and 2. It uses Field's metal, a eutectic alloy of Tin, Bismuth and Indium, whose melting temperature is 62 °C. The temperature of the melt (85 °C) is kept by a double-boiler ("bain-marie") technique. Table 1 gives the physical properties of Field's metal that have been previously measured (Hadj-Achour et al., 2021) and are used in present analysis to compute the aforementioned non dimensional numbers.

The GaLaD (for "Goutte à La Demande" *i.e.* Drop-On-Demand) experimental setup (*cf.* Fig. 1) has been modified to include an electromagnet (*cf.* Fig. 2) that allows for the opening of the stem-valve for a longer time thereby generating a jet (henceforth named JaLaD for "Jet à La Demande" *i.e.* Jet-On-Demand). The velocity of the jet is controlled by varying the pressure of the Nitrogen gas-supply. A sketch of the experimental set-up is shown on Fig. 3.

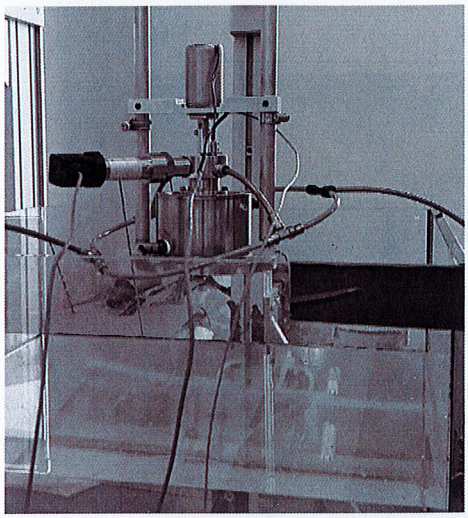

Fig. 2. JaLaD experimental Set-up.

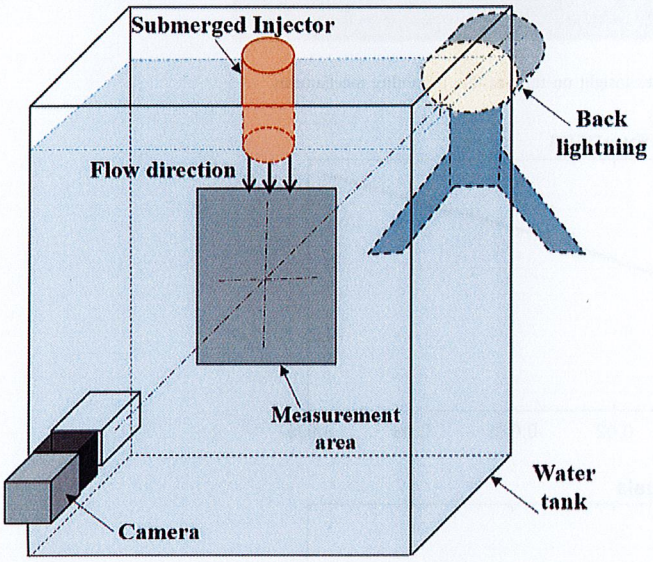

Fig. 3. JaLaD experimental set-up for liquid metal jet into water.

The size of the water pool is 50 cm × 50 cm × 40 cm and is heated to 40 °C. This choice stems from the initial liquid metal temperature set to 85 °C. To limit solidification impact during fragmentation, the pool temperature has to be increased up to the limit where droplets are still liquid when they touch the bottom, estimated, empirically, to be 50 °C. This corresponds to a contact temperature T_C of 75 °C, obtained by the following equation (neglecting convection),

$$T_C = \frac{E_L T_L + E_C T_C}{E_L + E_C} \tag{5}$$

where E_L and E_C are respectively the thermal effusivity ($\sqrt{k\rho C_p}$) of the Field's metal liquid droplet and ambient carrying water, T_C is the ambient carrying water pool temperature and T_L is the Field's metal liquid droplet temperature. Therefore a lower value, of 40 °C, has been used for the pool temperature in most experiments to ensure that the fragments do not coalesce on the bottom. Therefore, it is assumed that the jet remains liquid during its disintegration in the water but that the droplets solidify before they hit the bottom of the vessel, where they will be eventually collected to be sieved.

In the present work, two measurement techniques are used to study the jet disintegration. The first technique is high speed shadowgraphy.

Table 2
Experimental conditions for the high-speed shadowgraphy and the sieving experiments.

Test	D_0	Pressure	U_0 (m/s)	We_C	Oh	Re_L	SMD/D_0
D2P6	2 mm	6 bar	2.3	26	0.0039	3697	0.47
D2P10	2 mm	10 bar	2.8	39	0.0039	4527	0.29
D5P6	5 mm	6 bar	4.4	234	0.0025	16964	0.15
D5P10	5 mm	10 bar	4.8	281	0.0025	18958	0.11

Table 3
Mass measurements by sieving.

We	20 µm	50 µm	100 µm	500 µm	1 mm	2 mm	Total
26	0.3 g	0.9 g	10.9 g	34.7 g	60.7 g	13.4 g	120.4 g
39	0.6 g	1.2 g	24.7 g	59.2 g	23.9 g	45.8 g	132.9 g
234	0.4 g	1.7 g	15.5 g	23.2 g	60.7 g	30.6 g	132.1 g
281	1.1 g	2.4 g	19.2 g	33.0 g	57.3 g	11.6 g	124.6 g

Imaging is obtained thanks to a LED back lighting (PRIOLITE LED 400 equivalent to 400 W halogen light) and a phantom V701 high speed camera. The second system is simpler: it consists in a Retsch vibratory sieve shaker AS 200 which is used to separate the fragments according to their size. Each bin is thereafter weighted and the results recorded (in Table 3).

2.3. High speed shadowgraphy

Fig. 4 shows a sample shadowgraph. The pressure is imposed in the gas tank and measure of the tip penetration speed, obtained after image analysis, gives us an estimate of the jet velocity U_0 (*cf.* Fig. 5). This way of evaluating the liquid jet velocity is common in Fuel Coolant Interaction (FCI) experiments and will allow us to compare our results with previously published experimental results (Manickam et al., 2017; Li et al., 2017). Table 2 indicates the four different experimental conditions for the combined shadowgraph/sieving experiments that will be studied in present work. Note that, in present analysis, shadowgraph method is used no further (as the optical density of the spray prevents, for instance, direct measurement of the spray PDF by image analysis).

2.4. Sieving results

Table 3 indicates the result of the sieving of the solidified fragments for the four tests (summarized by their Weber number). The corresponding Mass PDF $\frac{1}{M_{tot}}\frac{dM}{d\log_{10}(D)}$ of the logarithm of the diameter $\log_{10}(D/D_0)$ is given on Fig. 6. It can be seen that, using the half-width height, for the lower Weber number experiments (*i.e.* $We \in [30, 40]$), most of the mass is in the range $D/D_0 \in [0.3, 1]$ (*i.e.* $\log_{10}(D/D_0) \in [-0.5, 0]$) while for the higher Weber number (*i.e.* $We \in [200, 300]$), most of the mass is in the range $D/D_0 \in [0.1, 0.6]$ (*i.e.* $\log_{10}(D/D_0) \in [-1, -0.2]$).

As in Hadj-Achour et al. (2021), the values of the Sauter Mean Diameters (SMD for short, this is the diameter of the droplet that has the same surface/volume ratio as the whole cloud) given in Table 2 are computed from Table 3 using Eq. (6).

$$SMD = \frac{1}{\sum_{i=0}^{N_s} x_i / \bar{D}_i} \tag{6}$$

where x_i is the mass fraction of sieve number i and $\bar{D}_i = \frac{D_i + D_{i+1}}{2}$ is the "average" bin sieve diameter and N_s the number of sieves used. Note that for the largest sieve (2mm), the $i+1^{th}$ sieve size (which does not exist and is only virtual) has been set to $1.8 \times D_0$ to account for droplets eventually generated by Rayleigh-Plateau instability. This has low impact on the SMD which gives more weight to the small droplets however (Likewise the non sphericity of larger solidified droplets has

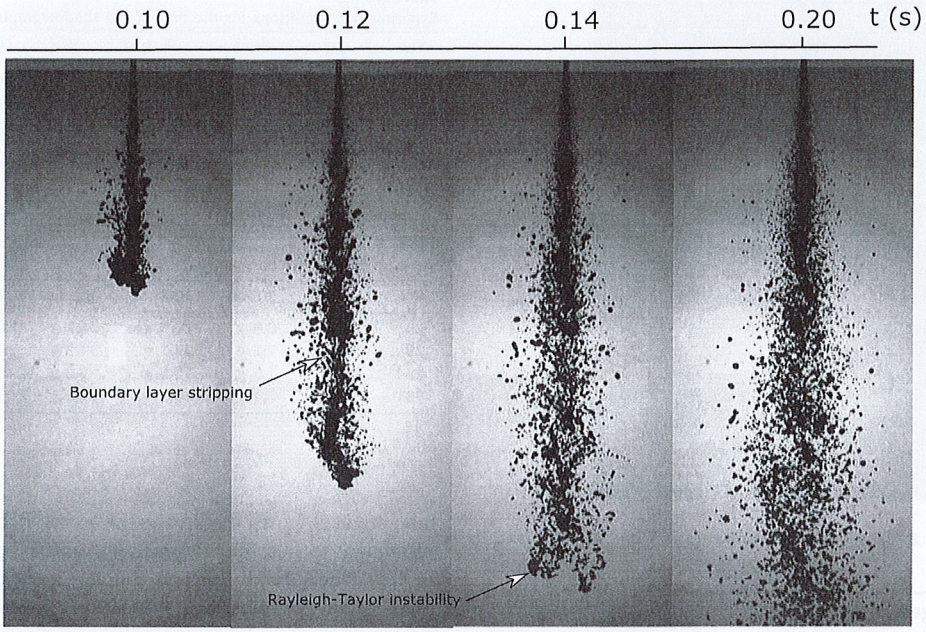

Fig. 4. Shadowgraph images for D2P6 experiment. It gives insight on the possible instability mechanisms.

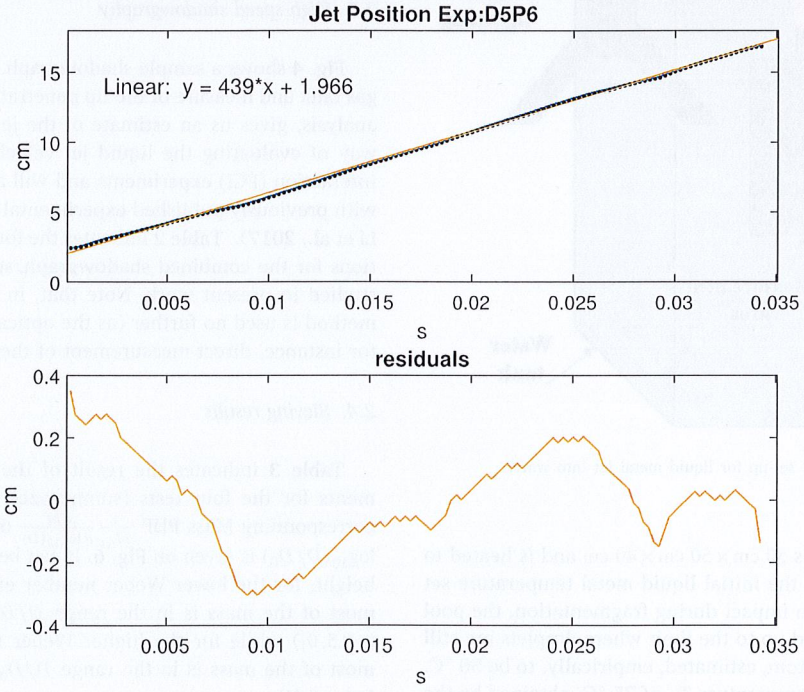

Fig. 5. Jet tip position for D2P6 experiment. Computing the slope allows for determining the jet velocity (here 439 cm/s). As for validation, it can be seen that the residuals show very small correlations.

low impact). Fig. 7 shows the evolution of SMD/D_0 ratio with Weber number. There appears to be a scaling

$$\frac{SMD}{D_0} \propto We^{-1/2} \tag{7}$$

Some other previously published results have also been included in Fig. 7. Note that they were mostly hot experiments where some vapor was produced. Note also that this scaling seems compatible with the data published in the review (Iwasawa and Abe, 2018) though the MMD is used instead of the SMD. This may suggest that Rayleigh–Taylor instability (*cf.* Eq. (25)) may be at play in the present fragmentation mechanism. This discussion is, however, left to next section.

3. Modeling of the experimental results

3.1. Inadequacy of single step instability mechanisms and turbulent scales

In this section, we propose to review some classical instability mechanisms that are usually associated to liquid fragmentation in FCI (Abe et al., 2004, 2006; Iwasawa and Abe, 2018) and compare their most amplified wavelengths to the size of the fragments, showing that these single step mechanisms cannot explain the size of the fragments. The following characteristic length scales are therefore computed: first, the (most amplified) wavelength λ_{KH} associated to the classical planar Kelvin–Helmholtz (*cf.* Eq. (8), in this classical model only surface

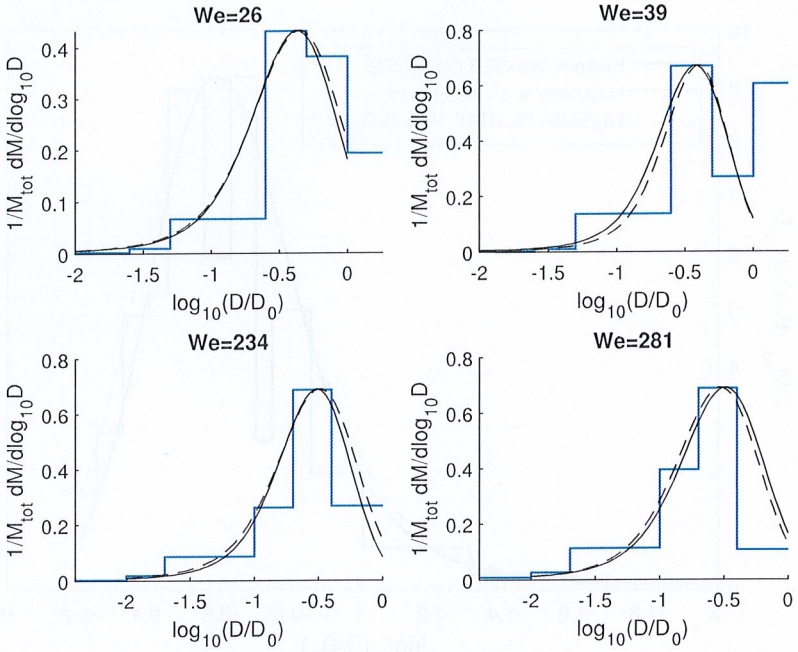

Fig. 6. Mass Distribution for present experiment. Fitting of the PDF with a log-stable model is represented as a black line for the We = 281 case. The dashed black line is the result of the model developed in the present work.

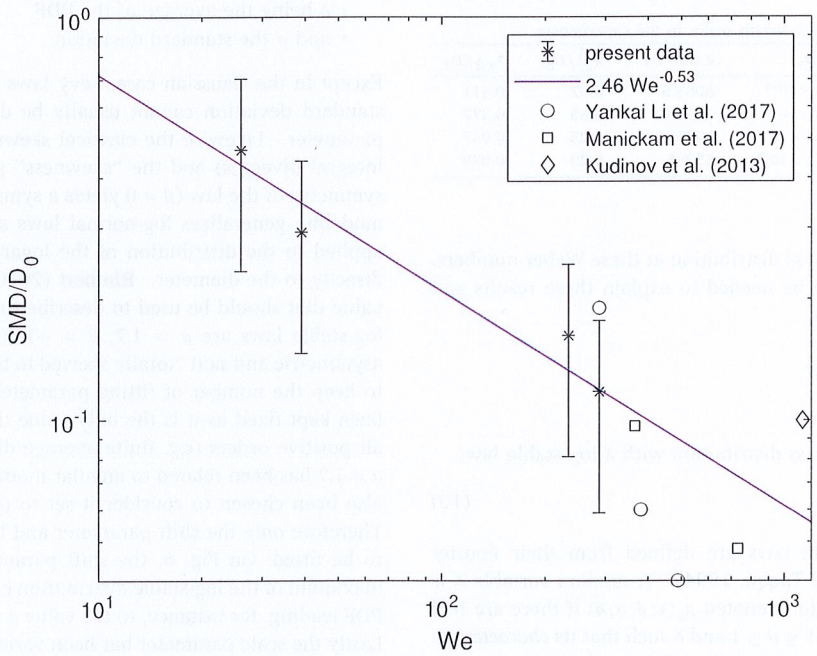

Fig. 7. Sauter Mean Diameter as a function of Weber number. The line is a power-law fitting of the data.

tension is included, the two fluids are perfect, of constant density and there is a sharp velocity jump at the interface), which is given by

$$\lambda_{KH} = \frac{3\pi\gamma\left(\rho_C + \rho_L\right)}{U_0^2 \rho_C \rho_L}. \tag{8}$$

Second, the most amplified wavelength $\lambda_{RT}^{(g)}$ of Rayleigh–Taylor instability (Chandrasekhar, 2013) is given by Eq. (9).

$$\lambda_{RT}^{(g)} = 2\pi\sqrt{\frac{3\gamma}{g\left(\rho_L - \rho_C\right)}} \tag{9}$$

where g is gravity acceleration (Iwasawa and Abe, 2018). Actually real acceleration g should be the jet local acceleration (or deceleration) but it is not easy to determine experimentally (being a second order time derivative of the jet position, it gives very noisy results) and is therefore not included here (but this idea will be used in the following). This results in a magnitude of $\lambda_{RT}^{(g)} \approx 2.6$ cm which can be ruled out except maybe, lately, at the tip of the jet (*cf.* Fig. 4 for t = 140 ms). It is therefore obvious that gravity is not the main driving force of present fragmentation mechanism (actually the Froude number $Fr = U_0/\sqrt{gD_0} \approx 10 \gg 1$). Last, it can be also interesting to compare these length scales with some characteristic turbulent length scales (*cf.* Appendix C). Table 4 summarizes the results of such order of magnitude computations. Comparatively it can be seen that none of the proposed instability mechanisms are in the range of the half-width of the mass distribution. Likewise, turbulence scales are so small that they do not

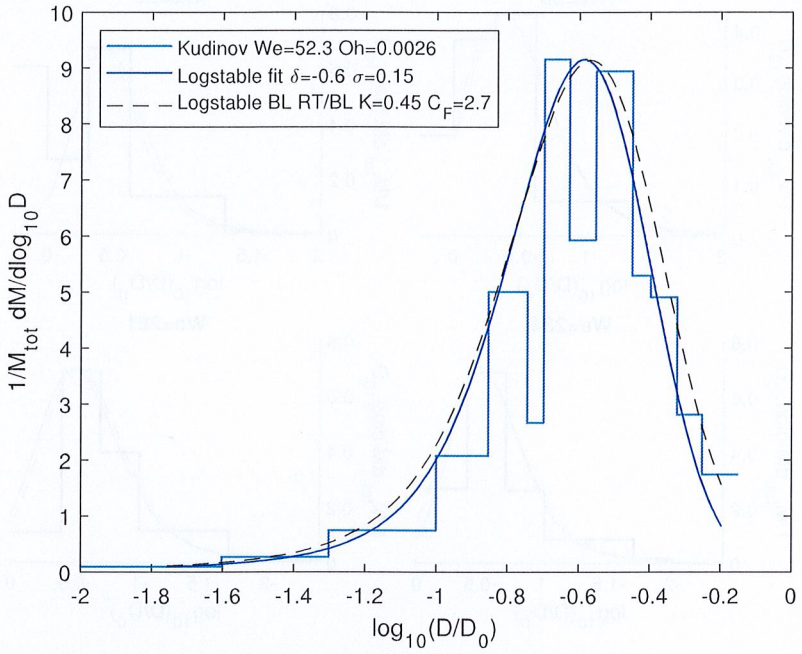

Fig. 8. Mass Distribution from Kudinov et al. (2013) DEFOR-A experiments with Bi_2O_3-WO_3 corium simulant melt.

Table 4
Instability and turbulence characteristic length scales in the experiments.

We	λ_S/D_0	λ_T/D_0	η/D_0	ϵ (m^2/s^3)	$\lambda_{RT}^{(f)}/D_0$	λ_{KH}/D_0
26	0.17	0.0351	1.8×10^{-3}	6083.5	0.67	0.411
39	0.15	0.0261	1.5×10^{-3}	10976	0.55	0.277
234	0.08	0.0055	4.48×10^{-4}	39753	0.23	0.047
281	0.08	0.0047	4.12×10^{-4}	55296	0.20	0.038

seem to be connected to the mass distribution at these Weber numbers. A new scenario will therefore be needed to explain these results and will be detailed in Section 3.3.

3.2. Fitting the mass distribution

3.2.1. Fitting procedure

Fig. 6 shows a fit to the mass distribution with a log-stable law:

$$\frac{1}{M_{tot}}\frac{dM}{d\log_{10}(D)} \hookrightarrow p_\alpha(x;\beta,\sigma,\delta) \tag{10}$$

Let us recall that Lévy stable laws are defined from their Fourier transform (Samorodnitsky and Taqqu, 1994): "A random variable X is said to have a stable distribution denoted $p_\alpha(x;\beta,\sigma,\delta)$ if there are real parameters $0<\alpha\leq 2$, $0<\sigma$, $-1\leq\beta\leq 1$ and δ such that its *characteristic function* (*i.e.* its Fourier transform) has the following form:

$$\hat{p}_\alpha(k;\beta,\sigma,\delta)=\exp\left(ik\delta-\sigma^\alpha|k|^\alpha\left[1+i(\text{sign}(k))\beta\omega(|k|,\alpha)\right]\right) \tag{11}$$

where

$$\omega(|k|,\alpha)=\begin{cases}\tan(\alpha\pi/2) & \text{if} \quad \alpha\neq 1\\ -2/\pi\log|k| & \text{if} \quad \alpha=1\end{cases} \tag{12}$$

"

Simply put, the four parameters are respectively, α, the stability index, governing the tail of the distribution, β, the "skewness" parameter, governing the symmetry of the law, δ, the shift parameter, governing the position of the maximum of the distribution and σ, the scale parameter, governing the width of the distribution. Gaussian laws are special cases of Lévy laws with parameters:

- $\alpha=2$,
- β being indifferent,
- δ being the average of the PDF
- and σ the standard deviation.

Except in the Gaussian case, Lévy laws are not square integrable, the standard deviation cannot usually be defined, hence the name scale parameter. Likewise the classical skewness cannot be computed (the integral diverges) and the "skewness" parameter mainly governs the symmetry of the law ($\beta=0$ yields a symmetric law). Note that present modeling generalizes log-normal laws and not Gaussian laws as it is applied to the distribution of the logarithm of the diameter and not directly to the diameter. Rimbert (2010) shows theoretically that the value that should be used to describe turbulence intermittencies using log-stable laws are $\alpha=1.7$, $\beta=-1$ (note that the distributions are asymmetric and said "totally skewed to the left" when $\beta=-1$). In order to keep the number of fitting parameters low, this value $\beta=-1$ has been kept fixed as it is the only value that leads to finite moments of all positive orders (*e.g.* finite average diameters). Moreover the value $\alpha=1.7$ has been related to angular momentum conservation and it has also been chosen to consider it set to this value in the present work. Therefore only the shift parameter and the scale parameters now need to be fitted. On Fig. 6, the shift parameter has been set so that the maximum of the log-stable distribution coincides with the experimental PDF leading, for instance, to the value $\delta=-0.55$ for the $We=281$ case. Lastly the scale parameter has been varied leading to the value $\sigma=0.24$ (also for $We=281$). It therefore seems that log-stable distribution are adequate to describe the mass distribution in this intermediate Weber number liquid–liquid spray.

3.2.2. Comparison with previous experiments

Figs. 8–14 show that this fitting process can also be applied to many data previously published for solidified fragments of liquid–liquid jets (Kudinov et al., 2013; Manickam et al., 2017; Li et al., 2017). Fig. 15 also shows the result of KROTOS test KA1 (Piluso et al., 2015; Cassiaut-Louis, 2015; Meignen et al., 2017) that involved prototypical corium. At CEA-CADARACHE, the KROTOS facility allows to perform integral tests with prototypical corium, i.e. using nuclear fuel UO_2. The KROTOS facility consists of three parts — furnace, release channel and test sections. Tungsten crucible is filled with prototypical corium powders and then is heated up to corium liquidus temperature (T> 2500 °C) with an overheating between 100 °C and 200 °C. Then the crucible is

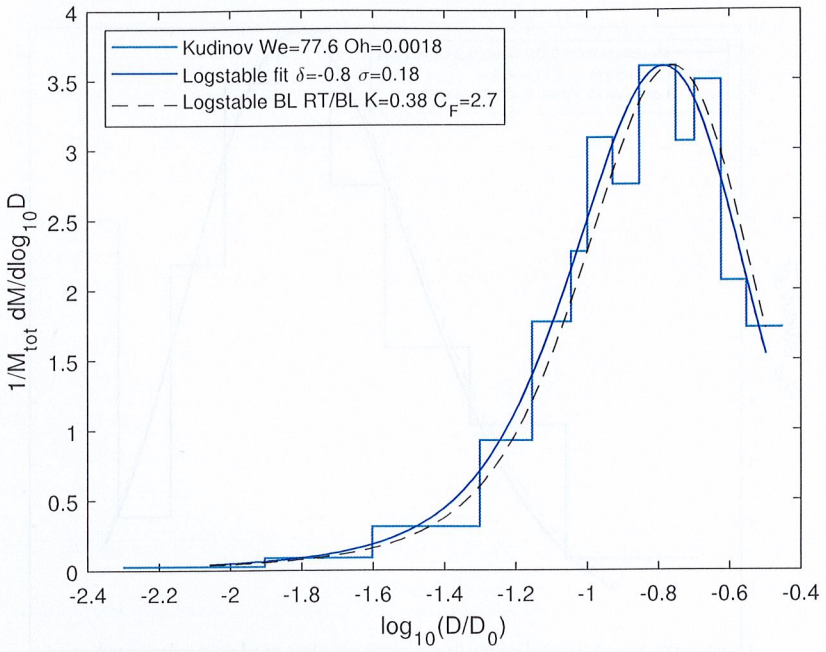

Fig. 9. Mass Distribution from Kudinov et al. (2013) DEFOR-A experiments with Bi_2O_3-WO_3 corium simulant melt.

released through a channel and a corium jet is formed with controlled parameter for corium jet diameter, speed, and temperature before the entrance into water. The test section is highly instrumented to follow fragmentation of the jet in conditions simulating the real reactor case conditions for the 3-phases (corium-steam-water) (Piluso et al., 2015; Cassiaut-Louis, 2015). Two kinds of tests have been performed in the frame of ICE program on KROTOS facility: premixing test and steam explosion test. This paper focuses on a premixing test performed on KROTOS facility: KROTOS KA-1. The main experimental parameters of KROTOS KA1 test were:

- corium mixture 80% UO_2 - 20% ZrO_2
- release temperature : 2710 °C
- jet diameter: 30 mm
- water temperature : 58 °C

The size of corium debris were between 200 μm and 8000 μm. The main class (32%wt) was between 2000 and 4000 μm. Details of the granulometry (and other relevant parameters) of KROTOS KA1 test are given in Appendix A.

3.3. "Computing" the mass distribution

The goal of this section is to build a model for the computation of the scale and the shift parameter.

In order to compute the scale and shift parameter, we can consider that the shift parameter set the scale of the large fragments whose size are mainly governed by the wave instability that develops at the interface between the two fluids while the scale parameter is mainly related to the "multiplier" of the cascade model and can be related to the ratio between the first wavelength and Rayleigh–Taylor instability wavelength developing on top of the wave.

3.3.1. Primary viscous shear instability

As has been seen in Table 4, the classical Kelvin–Helmholtz model (*cf.* Eq. (8)) predicts very short wavelengths that do not seem to be related to droplet sizes. We therefore propose to adapt here a model of boundary layer stripping based on a viscous shear instability that develop inside the Liquid phase. In order to estimate the thickness of the Liquid boundary layer, we can use a model developed by Girin (2018). First we assume that the boundary layer growths in the Carrier and Liquid phase are laminar and given by

$$\delta_C = K\frac{D_0}{Re_C^{*1/2}}, \tag{13}$$

$$\delta_L = K\frac{D_0}{Re_L^{*1/2}} \tag{14}$$

where K is a geometrical factor (which takes into account the location where the boundary layer thickness should be computed) and

$$Re_L^* = \frac{\rho_L(U_L - U_S)D_0}{\mu_L}, \tag{15}$$

$$Re_C^* = \frac{\rho_C U_S D_0}{\mu_C}, \tag{16}$$

U_S is the surface velocity. Then using a Karman-Polhausen-Walz approach (Schlichting and Gersten, 1961) using first order polynomials and using continuity of shear stress at the interface, the following relations can be established (details of the computation are given in Appendix B):

$$\delta_L = \frac{\mu_R^{2/3}}{\rho_R^{1/3}}\delta_C, \tag{17}$$

$$U_S = \frac{(\rho_R\mu_R)^{1/3}}{1+(\rho_R\mu_R)^{1/3}}U_L \tag{18}$$

In the present case, $\mu_R \approx 20$ and $\rho_R \approx 8$ which makes δ_C roughly one fourth of δ_L while $U_S \approx 0.84U_L$. Now the wavelength of the viscous shear instability is computed using $\delta_{BL} = \delta_C + \delta_L$ as the vorticity thickness in classical Rayleigh's model of planar viscous shear instability (Rayleigh, 1880; Charru, 2012) which gives

$$k_{S,max}\delta_{BL} = 0.4. \tag{19}$$

where $k_{S,max}$ is the most amplified wave-number of this viscous shear instability. After some simple algebra, this yields

$$\frac{\lambda_S}{D_0} = \frac{2\pi}{0.4}\left(1+\frac{\rho_R^{1/3}}{\mu_R^{1/3}}\right)(1+(\rho_R\mu_R)^{1/3})^{1/2}\frac{K}{\sqrt{Re_L}}, \tag{20}$$

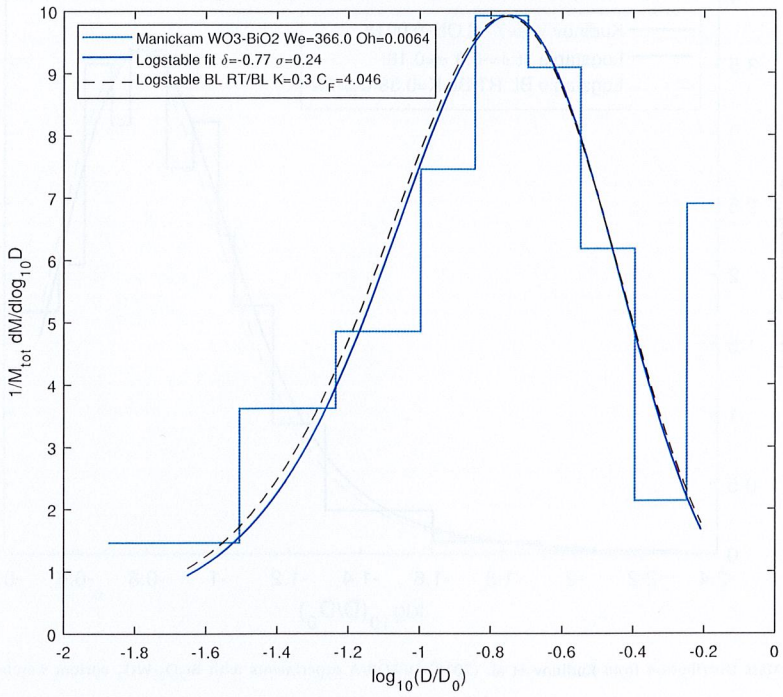

Fig. 10. Mass Distribution from Manickam et al. (2017) MISTEE Experiment with Bi_2O_3-WO_3 corium simulant melt.

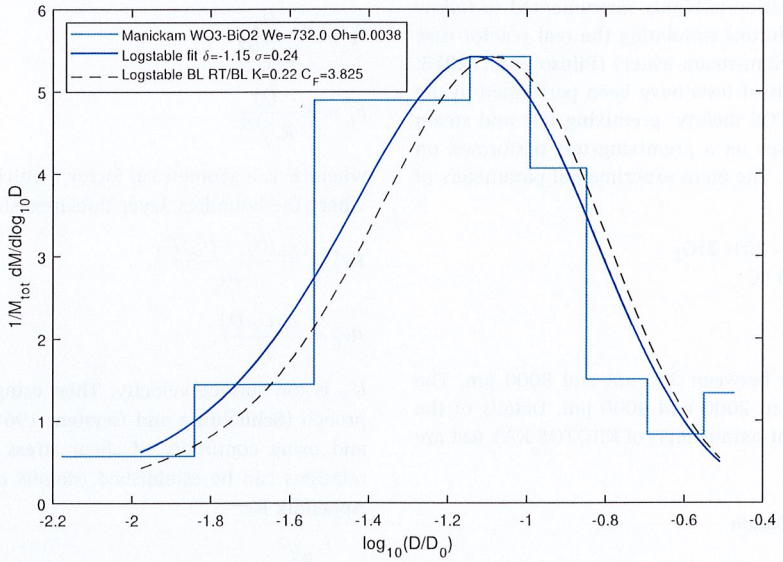

Fig. 11. Mass Distribution from Manickam et al. (2017) MISTEE Experiment with Bi_2O_3-WO_3 corium simulant melt.

where λ_S is the most amplified wavelength of this model; and in the present case

$$\frac{\lambda_S}{D_0} = 50.6\frac{K}{\sqrt{Re_L}}. \tag{21}$$

Note that this can also be related to O. Girin's "gradient instability" (Girin, 1985). O. Girin's result is important in our opinion as it pioneers the experimental and heuristic results of Hsiang & Faeth (Hsiang and Faeth, 1992) which relate the size of the droplets to the size of the boundary layer, but using instability theory and not qualitative arguments. In recent work of Girin (2018), let us emphasize that the boundary layer is assumed to be laminar as it is applied to the tip of the jet and is therefore a developing boundary layer. We can wonder if it is applicable in present experiment but looking at the geometry of the nozzle given in Fig. 1, the nozzle is very short and we do not believe that the boundary layers developing inside the nozzle have an impact on the jet fragmentation. This is different, for instance, from Eastwood et al. (2004) analysis where the surrounding flow was deliberately made turbulent. Turbulent cases reported in appendix of (Marmottant and Villermaux, 2004), where the liquid jet was deliberately made turbulent by using an array of turbulence promoters (*i.e.* steps), would eventually lead to other scaling than Eq. (14) but the geometries reported are actually quite different. Likewise, in many experiments used for comparison in present work, the jet is having a free-fall before impacting the water pool and we do not think that a turbulent boundary layer is developing before impact with water. To conclude this part, there has also been several recent analytical and numerical studies of shear instabilities in co-flowing jets and sheets (see Otto et al., 2013; Fuster et al., 2013; Ling et al., 2019 and references therein for instance) but none of them, as far as we have found, presented a simple

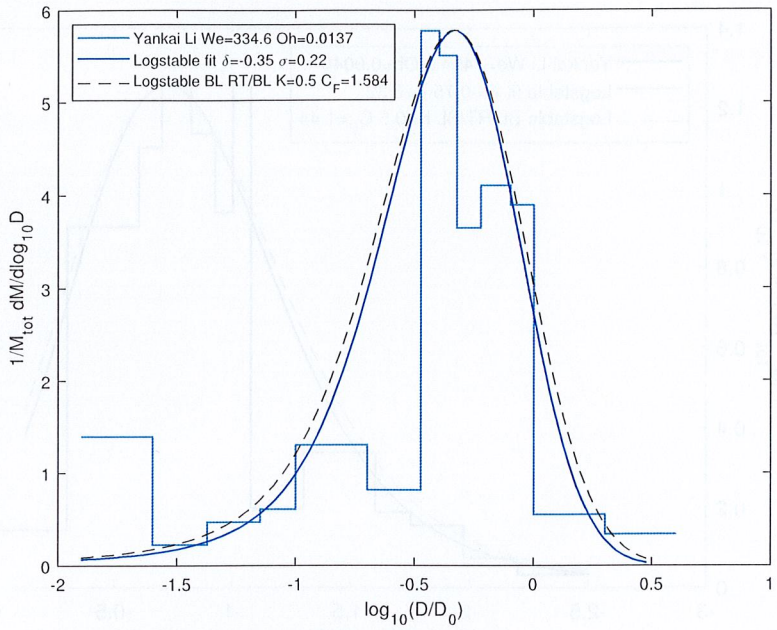

Fig. 12. Mass Distribution from Li et al. (2017) METRIC experiment with molten tin (Sn).

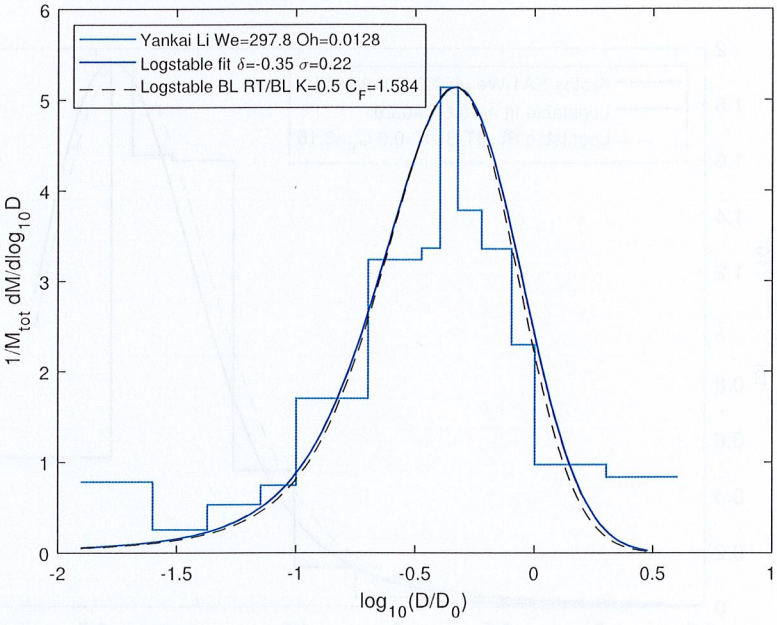

Fig. 13. Mass Distribution from Li et al. (2017) METRIC experiment with molten tin (Sn).

analytical formula similar to Eq. (20) that could be used for practical applications.

3.3.2. Secondary Rayleigh–Taylor instability

In the present model, Rayleigh–Taylor instability is applied as a second step to the wave generated during the first step. We therefore consider a secondary "droplet", whose diameter will be assumed to be $D_1 \approx \lambda_S$ (*cf.* Varga et al., 2003), and supersede its deceleration $f = dU_r/dt$ (where U_r is the relative velocity between the droplet and the surrounding fluid) to the gravity acceleration g in Eq. (9), using the classical approximation

$$\frac{\pi D_1^3}{6}\rho_L \frac{dU_r}{dt} \approx -\rho_C y^2 \frac{\pi D_1^2}{4} C_d U_r^2 \tag{22}$$

where y is the "droplet" extension due to its deformation by the flow (*cf.* Rimbert et al., 2020 for instance) which yields

$$f \approx \frac{3}{2}\frac{\rho_C}{\rho_L}\frac{y^2}{D_1} C_d U_0^2 \tag{23}$$

assuming $U_r \approx U_0$. We then get

$$\frac{\lambda_{RT}^{(f)}}{D_1} \approx \pi \frac{1}{y}\sqrt{\frac{16\gamma}{C_d \rho_C U_0^2 D_1}} \tag{24}$$

where $\lambda_{RT}^{(f)}$ is the Rayleigh–Taylor most amplified wavelength computed using the liquid patch deceleration f instead of gravity acceleration g. Now if we use again the approximation $D_1 \approx \lambda_S$, one gets

$$\frac{\lambda_{RT}^{(f)}}{D_0} \approx \pi \frac{1}{y}\sqrt{\frac{8}{C_d We}}\sqrt{\frac{D_0}{\lambda_S}} \tag{25}$$

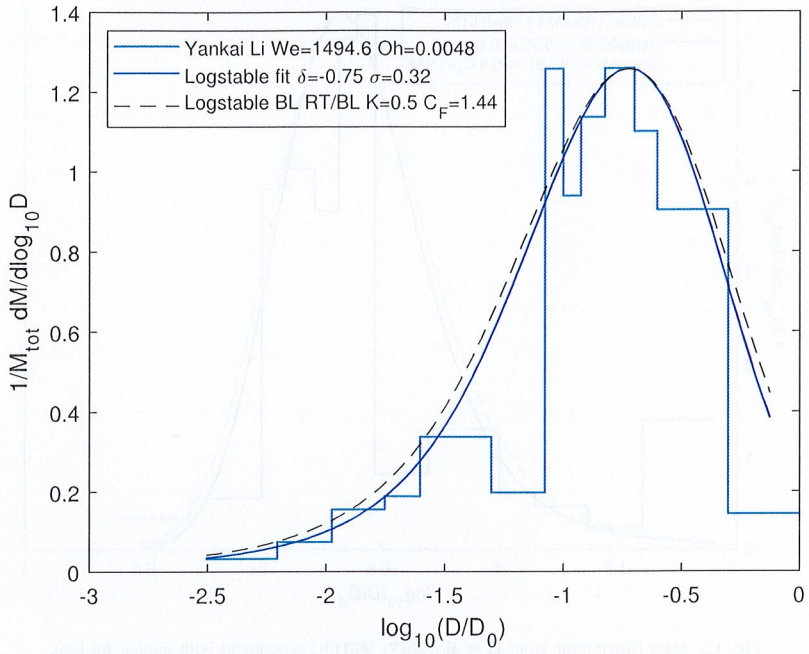

Fig. 14. Mass Distribution from Li et al. (2017) METRIC experiment with molten tin (Sn).

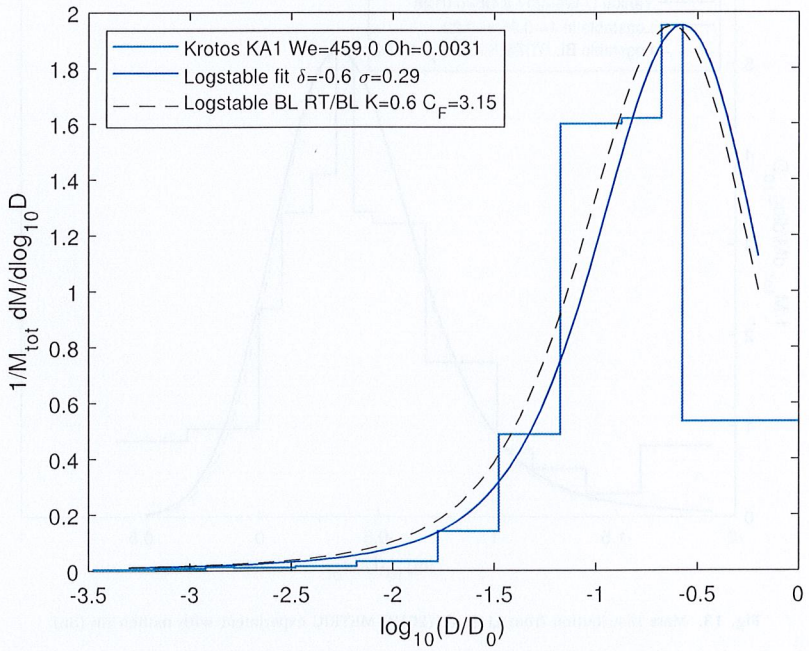

Fig. 15. Mass Distribution KROTOS Test KA1 (Piluso et al., 2015).

The parameters of the log-stable distribution are therefore computed using

$$\delta = \log_{10} \frac{\lambda_S}{D_0}, \tag{26}$$

$$\sigma = \log_{10} \frac{\lambda_{RT}^{(f)}}{\lambda_S} \tag{27}$$

and Eqs. (20) and (25). Note that the idea of relating some parameters of the self-similar fragmentation equation to the instability wavelengths (or the ratio of instability wavelengths), seen as the first (or second) step of the "cascade", has been previously attempted by Gorokhovski et al. (2009) in a numerical model, taking inspiration from the works of Varga et al. (2003). However, it was applied to the number distribution of droplet and not to their mass distribution.

To conclude this part, it seems that the log-stable Mass PDF that has been found as an asymptotics to the self-similar fragmentation equation in Rimbert and Séro-Guillaume (2004) is also valid in this two-step cascade model (viscous shear instability succeeded by Rayleigh–Taylor instability). Actually, the self-similar fragmentation equation is also known, in chemical engineering, as the homogeneous fragmentation equation (see Kostoglou, 2003 for instance) without resorting to "cascade" arguments. This may explain why, in this rather low Weber number case, the asymptotic result may still be valid whereas the "cascade" is actually quite short as two steps are only required and high-speed video footage do not show droplets breaking up again and again. Actually, self-similar solutions are often observed in nature when

Table 5
Fitting of the parameters C_F, K and modification of the viscosity needed to obtain log stable mass PDF close to the experiments using eq. (26) and (27). Material properties used are respectively for Bi_2O_3-WO_3, UO_2-ZrO_2 and Sn: 13.2 mPa s, 10 mPa s and 2 mPa s for dynamic viscosity; 6728 kg/m^3, 7121 kg/m^3, 6800 kg/m^3 for density and 0.18 N/m, 0.8 N/m, 0.57 N/m for surface tension.

Name	We	Oh	$C_F = C_d y^2$	K	Viscosity	Note
D2P6	26	0.001	2.35	0.55	×2	Field's metal
D2P10	39	0.001	2.35	0.45	×2	Field's metal
Kudinov et al.	52	0.003	2.7	0.45	×1	Bi_2O_3-WO_3, low subcooling
Kudinov et al.	78	0.002	2.7	0.38	×1	Bi_2O_3-WO_3, low subcooling
D5P6	234	0.001	3.15	0.57	×2	Field's metal
D5P10	281	0.001	2.9	0.55	×2	Field's metal
Yankai Li et al.	298	0.013	1.58	0.50	×40	Sn, T_m = 612 °C, local vapor explosion
Yankai Li et al.	334	0.014	1.44	0.50	×40	Sn, T_m = 803 °C, local vapor explosion
Manickam et al.	366	0.006	3.15	0.35	×2	Bi_2O_3-WO_3, high subcooling
Krotos KA1	459	0.003	3.15	0.6	×4	UO_2-ZrO_2(80%,20%), T_m = 2500 K
Manickam et al.	732	0.004	3.8	0.22	×2	Bi_2O_3-WO_3, high subcooling
Yankai Li et al.	1495	0.005	1.44	0.50	×40	Sn, T_m = 997 °C, local vapor explosion

the boundary conditions (here, for the fragmentation equation: the very large and very small scales) can be somehow forgotten.

Moreover, though this part is entitled "Computing" the distribution, either the values of y or C_d (or rather the product $C_F = C_d y^2$) and K need to be fitted in the end (though the values used are in the appropriate range *cf.* Table 5). There are therefore two fitting parameters: C_F which is a friction parameter and K which is a geometrical parameter governing boundary layer development.

3.4. Comparison with previously published results

Figs. 8–15 have already shown that it was possible to fit the mass distribution using log-stable laws. These figures also include as dashed line results of the present model. However some slight (and sometime not that slight) fitting of the parameters C_F and K have been needed in order to best approximate the mass distribution of the fragments with the presented model. Table 5 summarizes the results of this fitting procedure. Note that the viscosity of the melt have also been slightly modified when deemed necessary. This modification is here empirical, but could be related to either solidification or oxidation mechanism that are not included in present model. This shows the importance of knowing the material properties in details in order to predict precisely this fragmentation process.

From Table 5, it can be seen that the variation of the fitting parameters are rather small with $K \approx 0.5$ and $C_F = C_d y^2$ slowly increasing from 2.3 to 3.8 when Weber number increases. Note that this order of magnitude for C_F is compatible with the values reported in Qaddah et al. (2019) for geophysics applications. MISTEE Data provided by Kudinov et al. need very few modifications of the parameters. Moreover, the viscosity value did not need to be modified in any way, in agreement with the fact that they used an oxide melt (Bi_2O_3-WO_3) which therefore rules out oxidation. KROTOS KA1 experiments also show good agreement with present model. Uncertainty on the material properties of corium is, as usual, a problem as it is very difficult to make precise measurements on a melt close to 3000 K. Two sets of experimental results seem to show discrepancies that result in a modification of the fitting parameters. Experimental results of Yankai Li et al. used very hot liquid tin with melt temperature ranging from 612 °C to 997 °C. Vaporization effects are therefore expected to be important and some localized vapor explosions have been reported by the authors. This is a known phenomenon for tin above 300 °C (Dullforce et al., 1976; Matsumura and Nariai, 1996) when the subcooling is high (which is the case in these experiments as $\Delta T_{sub} \approx -77$ °C). They did not observe global vapor explosions however. Moreover, the PDF given by Yankai Li et al. are not very smooth and the peak of small droplets that are present on the PDF (*cf.* Figs. 12 and 13) can be interpreted as coming from the localized vapor explosion that they reported. This may explain why this is the only case where the viscosity was needed to be multiplied fortyfold! Note also that it has been chosen to use the property of water at room temperature for the carrier phase in all these analyses but in this specific case, using a much smaller density (that of the surrounding vapor) would lead to different result (in that case there is no need to multiply the viscosity fortyfold but then, the vapor density becomes the unknown parameter). Experimental results of Manickam et al. that have been considered here, involve Bi_2O_3-WO_3 mixture in highly subcooled water ($\Delta T_{sub} = -80$ °C). They report (Manickam et al., 2017) that in this condition the solidified glass beads can fragment yet another time when they cool down (due to some thermal cracking). This may explain why the parameters are so different in this case. Interestingly enough, the global shape of the PDF (*i.e.* the log-stable shape) seems to be preserved even in these limit experiments.

4. Conclusion

In this work, it has been shown, by sieving solidified fragments, that for a moderately low Weber number liquid–liquid spray, the mass distribution follows a log-stable law. These laws were introduced (Rimbert and Séro-Guillaume, 2004) as asymptotic solution to the self-similar fragmentation equation. This equation is usually believed to be a mathematical translation of the recurrent "cascade" models (stemming from Richardson's idealization of turbulence) whereas, in the present case, the cascade seems to be far from developed: no drop seems to divide more than once or twice on the video footage that we examined (see for instance Kewalramani et al., 2022 but where another transparent fluid has been injected). Nevertheless, it seems possible to compute all the parameters of the distribution (or rather an approximation of their value) by considering a self-similar cascade of instability: the first step being given by boundary layer stripping/viscous shear instability and the second step being given by Rayleigh–Taylor instability. This model has then been compared with previously published experiments in the field of Fuel Coolant Interaction study, showing rather good agreement. Disagreement can be related to either high vapor production or ternary thermal fragmentation of the solid fragments during cooling.

Let us emphasize that corium thermophysical properties are still partially known and will play an important role in the fragmentation process in the real case of a nuclear severe accident. It could be useful to provide reliable corium thermophysical properties such as density, surface tension and viscosity to enhance modeling of fragmentation process. Likewise, as these properties (viscosity, surface tension, ...*etc.*) can be modified by both liquid oxidation or solidification, the coupling between these processes should be another important topic of future investigations.

Moreover, nothing seems to prevent application of present model to more classical liquid–gas configurations. Actually, during the revision of present work, the ADAM method (Jackiw and Ashgriz, 2023) has been proposed for air-blast atomizers and shows similarities with present work (the main differences are that they use a mass log-normal distribution, a simpler shear instability formula and a different secondary instability based on a detailed bag breakup mechanism). This is however, left for future considerations.

Table A.6
Mass measurement for KROTOS KA1. The percentage indicates the mass found in the relevant sieve size (meaning that 18.52% of the mass was in the greater than 8mm sieve).

10 μm	20 μm	36 μm	50 μm	0.1 mm	0.2 mm	0.5 mm	1 mm	2 mm	4 mm	6.3 mm	8 mm
0.05%	0.1%	0.11%	0.17%	0.27%	0.79%	2.77%	9.72%	31.93%	21.66%	13.91%	18.52%

CRediT authorship contribution statement

Nicolas Rimbert: Conception and design of study, Acquisition of data, Analysis and/or interpretation of data, Writing – original draft, Writing – review & editing. **Miloud Hadj-Achour:** Conception and design of study, Acquisition of data, Analysis and/or interpretation of data, Writing – original draft, Writing – review & editing. **Bowen Ji:** Analysis and/or interpretation of data, Writing – original draft. **Gagan Kewalramani:** Writing – review & editing. **Alexandre Labergue:** Acquisition of data. **Yvan Dossmann:** Writing – review & editing. **Michel Gradeck:** Conception and design of study. **Pascal Piluso:** Acquisition of data. **Renaud Meignen:** Conception and design of study, Analysis and/or interpretation of data, Writing – original draft.

Declaration of competing interest

The authors declare that they have no known competing financial interests or personal relationships that could have appeared to influence the work reported in this paper.

Data availability

Data will be made available on request.

Acknowledgments

The work was done under the research program on nuclear safety and radioprotection (RSNR) and received funding from French government managed by the Agence Nationale de la Recherche (ANR), France under Future Investments Program (PIA), research grant No: ANR-10-RSNR-01. All authors approved the version of the manuscript to be published.

Appendix A. KROTOS KA1 Data

Details can be found in Piluso et al. (2015), Cassiaut-Louis (2015), Meignen et al. (2017). The following parameters are used in the present modeling:

$$D_0 = 30 \text{ mm} \quad \rho_C = 1000 \text{ kg/m}^3 \quad \rho_L = 7121 \text{ kg/m}^3 \tag{A.1}$$

$$\mu_L = 10 \text{ mPa s} \quad \mu_C = 1 \text{ mPa s} \quad \gamma = 0.8 \text{ N m}^{-1} \tag{A.2}$$

$$U_0 = 3.5 \text{ m/s} \quad We = 459 \tag{A.3}$$

Table A.6 gives the resulting granulometry that has been measured out of these 3193.7 g of corium melt.

Appendix B. Girin's double boundary layer model

We do not need all the developments found in Girin (2018) here. The main result stems from the equality of shear stress at the interface which reads

$$\tau_I \approx \mu_L \frac{U_L - U_S}{\delta_L} \approx \mu_C \frac{U_S}{\delta_C} \tag{B.1}$$

where a first linearization (*i.e.* first order polynomial) has been used to compute the velocity gradient. Using Eq. (13) and (14) in (B.1) leads to

$$\mu_L Re_L^{*1/2}(U_L - U_S) = \mu_C Re_C^{*1/2} U_S \tag{B.2}$$

But (13) and (14) also imply

$$\frac{Re_L^{*1/2}}{Re_C^{*1/2}} = \frac{\rho_L}{\rho_C}\frac{U_L - U_S}{U_S}\frac{\mu_C}{\mu_L} = \frac{\rho_R}{\mu_R}\frac{U_L - U_S}{U_S} \tag{B.3}$$

Combining both (B.2) and (B.3) leads to (17) and (18).

Appendix C. Estimates of some turbulence length scales

To compute them, the average turbulent kinetic energy dissipation rate ε is needed. It is estimated as usual (Tennekes and Lumley, 1972) through Eq. (C.1)

$$\varepsilon \cong \frac{u'^3}{L_{\text{int}}}, \tag{C.1}$$

where u' represents the fluctuating velocity around the statistical average (using Reynolds decomposition) and L_{int} is the integral scale of turbulence, estimated to be of the order of magnitude of the jet diameter. This allows for the computation of Taylor's characteristic turbulent length scale and Kolmogorov's length scale through Eq. (C.2) and (C.3).

$$\lambda_T = \sqrt{20\nu\frac{k}{\varepsilon}} \tag{C.2}$$

$$\eta \cong \left(\frac{\nu^3}{\varepsilon}\right)^{1/4} \tag{C.3}$$

In either Eq. (C.1) or Eq. (C.2), the turbulent kinetic energy k is computed assuming that $u' \approx U$ which is usually assumed true for turbulent jets.

References

Abe, Y., Kizu, T., Arai, T., Nariai, H., Chitose, K., Koyama, K., 2004. Study on thermal-hydraulic behavior during molten material and coolant interaction. Nucl. Eng. Des. 230 (1–3), 277–291.

Abe, Y., Matsuo, E., Arai, T., Nariai, H., Chitose, K., Koyama, K., Itoh, K., 2006. Fragmentation behavior during molten material and coolant interactions. Nucl. Eng. Des. 236 (14–16), 1668–1681.

Amirzadeh, A., Raessi, M., Chandra, S., 2013. Producing molten metal droplets smaller than the nozzle diameter using a pneumatic drop-on-demand generator. Exp. Therm Fluid Sci. 47, 26–33.

Beale, J.C., Reitz, R.D., 1999. Modeling spray atomization with the Kelvin-Helmholtz/Rayleigh-Taylor hybrid model. At. Spray. 9 (6).

Cassiaut-Louis, N., 2015. Réalisation de l'essai KA-1 dans le cadre du projet RSNR-ICE. Tech. Rep. RSNR-ICE/LIV/2015-12, CEA/DEN/CAD/DTN/SMTA/LPMA.

Chandrasekhar, S., 2013. Hydrodynamic and Hydromagnetic Stability. Courier Corporation.

Charru, F., 2012. Instabilités Hydrodynamiques. EDP sciences.

Dombrowski, N., Johns, W., 1963. The aerodynamic instability and disintegration of viscous liquid sheets. Chem. Eng. Sci. 18 (3), 203–214.

Dullforce, T., Buchanan, D., Peckover, R., 1976. Self-triggering of small-scale fuel-coolant interactions: I. experiments. J. Phys. D: Appl. Phys. 9 (9), 1295.

Eastwood, C.D., Armi, L., Lasheras, J., 2004. The breakup of immiscible fluids in turbulent flows. J. Fluid Mech. 502, 309–333.

Fuster, D., Matas, J.-P., Marty, S., Popinet, S., Hoepffner, J., Cartellier, A., Zaleski, S., 2013. Instability regimes in the primary breakup region of planar coflowing sheets. J. Fluid Mech. 736, 150–176.

Gelfand, B., 1996. Droplet breakup phenomena in flows with velocity lag. Prog. Energy Combust. Sci. 22 (3), 201–265.

Girin, O., 1985. Hydrodynamic instability and regimes of fragmentation of drops. J. Eng. Phys. 48 (5), 560–564.

Girin, O.G., 2018. Model of the fuel jet primary atomization and aerodynamics of spray formation at high-pressure injection in a diesel engine. At. Spray. 28 (3).

Gorokhovski, M., Jouanguy, J., Chtab-Desportes, A., 2009. Stochastic model of the near-to-injector spray formation assisted by a high-speed coaxial gas jet. Fluid Dyn. Res. 41 (3), 035509.

Gorokhovski, M., Saveliev, V., 2003. Analyses of Kolmogorov's model of breakup and its application into Lagrangian computation of liquid sprays under air-blast atomization. Phys. Fluids 15 (1), 184–192.

Hadj-Achour, M., Rimbert, N., Gradeck, M., Meignen, R., 2021. Fragmentation of a liquid metal droplet falling in a water pool. Phys. Fluids 33 (10), 103315.

Hsiang, L.-P., Faeth, G.M., 1992. Near-limit drop deformation and secondary breakup. Int. J. Multiph. Flow. 18 (5), 635–652.

Iwasawa, Y., Abe, Y., 2018. Melt jet-breakup and fragmentation phenomena in nuclear reactors: A review of experimental works and solidification effects. Prog. Nucl. Energy 108, 188–203.

Jackiw, I.M., Ashgriz, N., 2023. Aerodynamic droplet atomization model (ADAM). J. Fluid Mech. 958, A2.

Kewalramani, G., Ji, B., Dossmann, Y., Gradeck, M., Rimbert, N., 2022. Experimental analysis of Lagrangian paths of drops generated by liquid/liquid sprays. Exp. Fluids 63 (9), 147.

Kida, S., 1991. Log-stable distribution and intermittency of turbulence. J. Phys. Soc. Japan 60 (1), 5–8.

Kolmogorov, A.N., 1941. On the lognormal distribution law of the dimensions of particles under pulverization. In: Doklady of the Akademy of Sciences of the USSR, Vol. 31. pp. 99–101.

Kostoglou, M., 2003. Exact self-similar solutions to the fragmentation equation with homogeneous discrete kernel. Physica A 320, 84–96.

Kudinov, P., Karbojian, A., Tran, C.-T., Villanueva, W., 2013. Agglomeration and size distribution of debris in DEFOR-A experiments with Bi2O3–WO3 corium simulant melt. Nucl. Eng. Des. 263, 284–295.

Li, Y., Wang, Z., Lin, M., Zhong, M., Zhou, Y., Yang, Y., 2017. Experimental studies on breakup and fragmentation behavior of molten tin and coolant interaction. Sci. Technol. Nucl. Installations 2017.

Ling, Y., Fuster, D., Tryggvason, G., Zaleski, S., 2019. A two-phase mixing layer between parallel gas and liquid streams: multiphase turbulence statistics and influence of interfacial instability. J. Fluid Mech. 859, 268–307.

Mandelbrot, B.B., 1982. The Fractal Geometry of Nature. Freeman.

Manickam, L., Bechta, S., Ma, W., 2017. On the fragmentation characteristics of melt jets quenched in water. Int. J. Multiph. Flow. 91, 262–275.

Marmottant, P., Villermaux, E., 2004. On spray formation. J. Fluid Mech. 498, 73–111.

Matsumura, K., Nariai, H., 1996. Self-triggering mechanism of vapor explosions for a molten tin and water system. J. Nucl. Sci. Technol. 33 (4), 298–306.

Meignen, R., Piluso, P., Rimbert, N., 2017. Outcomes of the french ICE project on fuel coolant interaction. In: 17th International Topical Meeting on Nuclear Reactor Thermal Hydraulics. NURETH-17, p. 16.

Novikov, E., Dommermuth, D., 1997. Distribution of droplets in a turbulent spray. Phys. Rev. E 56 (5), 5479.

Otto, T., Rossi, M., Boeck, T., 2013. Viscous instability of a sheared liquid-gas interface: Dependence on fluid properties and basic velocity profile. Phys. Fluids 25 (3), 032103.

Pilch, M., Erdman, C., 1987. Use of breakup time data and velocity history data to predict the maximum size of stable fragments for acceleration-induced breakup of a liquid drop. Int. J. Multiph. Flow. 13 (6), 741–757.

Piluso, P., Cassiaut-Louis, N., Fouquart, P., Brayer, C., Tyrpek, V., Gueneau, C., Alpettaz, T., Gossé, S., 2015. ICE program: the CEA experimental program devoted to FCI studies with prototypical corium. In: The 7th European Review Meeting on Severe Accident Research. ERMSAR-2015.

Qaddah, B., Monteux, J., Clesi, V., Bouhifd, M.A., Le Bars, M., 2019. Dynamics and stability of an iron drop falling in a magma ocean. Phys. Earth Planet. Inter. 289, 75–89.

Rayleigh, L., 1880. On the stability, or instability, of certain fluid motions. Proc. Lond. Math. Soc. 9, 57–70.

Reitz, R.D., 1987. Modeling atomization processes in high-pressure vaporizing sprays. At. Spray. Technol. 3 (4), 309–337.

Rimbert, N., 2010. Simple model for turbulence intermittencies based on self-avoiding random vortex stretching. Phys. Rev. E 81 (5), 056315.

Rimbert, N., Escobar, S.C., Meignen, R., Hadj-Achour, M., Gradeck, M., 2020. Spheroidal droplet deformation, oscillation and breakup in uniform outer flow. J. Fluid Mech. 904.

Rimbert, N., Séro-Guillaume, O., 2003. Extension of the Kida law in turbulence. C. R. Méc. 331 (11), 775–782.

Rimbert, N., Séro-Guillaume, O., 2004. Log-stable laws as asymptotic solutions to a fragmentation equation: application to the distribution of droplets in a high Weber-number spray. Phys. Rev. E 69 (5), 056316.

Saito, S., Abe, Y., Koyama, K., 2017. Flow transition criteria of a liquid jet into a liquid pool. Nucl. Eng. Des. 315, 128–143.

Samorodnitsky, G., Taqqu, M., 1994. Non-Gaussian Stable Processes: Stochastic Models with Infinite Variance. Chapman ft Hall, London.

Schertzer, D., Lovejoy, S., 1987. Physical modeling and analysis of rain and clouds by anisotropic scaling multiplicative processes. J. Geophys. Res.: Atmos. 92 (D8), 9693–9714.

Schlichting, H., Gersten, K., 1961. Boundary Layer Theory. Springer.

Tennekes, H., Lumley, J.L., 1972. A First Course in Turbulence. MIT Press, p. 300.

Vallon, R., Abid, M., Anselmet, F., 2021. Multimodal distributions of agricultural-like sprays: A statistical analysis of drop population from a pressure-atomized spray. Phys. Rev. Fluids 6 (2), 023604.

Varga, C.M., Lasheras, J.C., Hopfinger, E.J., 2003. Initial breakup of a small-diameter liquid jet by a high-speed gas stream. J. Fluid Mech. 497, 405–434.

Villermaux, E., Marmottant, P., Duplat, J., 2004. Ligament-mediated spray formation. Phys. Rev. Lett. 92, 074501.